Automating Robotic Micro-Assembly of Fluidic Chips and Single Fiber Compression Tests Based-on $XY\Theta$ Visual Measurement With High-Precision Fiducial Markers

Antoine Andre, Olivier Lehmann, Jason Govilas, Guillaume Laurent, Hamdi Saadana, Patrick Sandoz, Vladimir Gauthier, Alexis Lefevre, Aude Bolopion, Joel Agnus, et al.

Automating Robotic Micro-Assembly of Fluidic Chips and Single Fiber Compression Tests based-on $XY\Theta$ Visual Measurement with High-Precision Fiducial Markers

Antoine N. André*, Olivier Lehmann*, Jason Govilas*, Guillaume J. Laurent, Hamdi Saadana, Patrick Sandoz, Vladimir Gauthier, Alexis Lefevre, Aude Bolopion, Joël Agnus, Vincent Placet, Cédric Clévy (* Equally contributing first authors)

Abstract

At small scales, automating robotic tasks such as assembly, force/displacement characterization, positioning, etc., appear to be particularly limited. This is due to the lack of sufficiently performing and easy-to-implement multi-degrees-of-freedom measurement systems able to measure the relative pose between micro-parts. In order to address this issue, a measurement method based on High-Precision fiducial markers (named HP code) is proposed. This measurement method combines a periodic pattern (providing high resolution by phase-based computation) with more regular QR codes (bringing versatile implementations and a quick detection). The design and method to efficiently locate these HP codes are presented in this paper. Experimental investigations demonstrate ultra-high resolution: 2 nm and 5 µrad along X, Y and Θ respectively (i.e. one thousandth of a pixel typically). The method is designed to be scalable as well as self-calibrated and to provide high robustness and high versatility. Two typical challenging applications in the field of microrobotics are automated to demonstrate these disruptive performances and the easy-to-implement capability of the method: (1) the automated assembly of two micro-fluidic chips through visual servoing with an achieved positioning accuracy below 50 nm, and (2) the automated micromechanical characterization of single fibers achieved by the integration of HP codes into a compliant structure enabling simultaneous micro-force and displacement sensing capabilities. These achievements highlight the versatility of the method and open the door to the rapid automation of high-quality robotic tasks at the micro scale.

Note to Practitioners

The motivation for this work/study is based on the fact that many application areas are extensively orienting towards microrobotic systems to perform precise tasks with versatility. However, at the micro scale, many disturbances such as the effects of climate change strongly affect this precision. This problem is amplified by the fact that sensors cannot be easily integrated, either by lack of space or by the lack of measurement systems available. Vision-based approaches are widespread at this scale and appear very promising to measure the relative pose between micro-parts. Nevertheless, existing vision-based approaches like digital image correlation are both scale and texture dependent. Due to the lack of space, they are also difficult to use in practice at small scales for high resolution measurement. The main contribution of this paper lies in the capability to achieve ultra-high resolution measurements. For that, a structure based on High-Precision fiducial markers (named HP codes) is proposed and requires few and simple settings while achieving very high resolution both in position and orientation, typically down to one thousandth of a pixel and a few micro radians, respectively. It provides an off-the-shelf solution, versatile, easy to implement and achieves high resolution measurements in the plane (XYΘ). HP codes are applicable to a wide range of applications such as tracking of a component/part of a mobile or deformable system, visual servoing of microrobots, positioning of samples, assembly of components or even mechanical characterization. A free distribution of the library is available online at `https://projects.femto-st.fr/vernier/`.

Authors are with the FEMTO-ST Institute, UMR CNRS 6174, Univ. Bourgogne Franche-Comté, 25000 Besançon, France.

Keywords

micro-assembly, force-displacement measurement, microrobotics, fluidic chip assembly, single fiber compression, computer vision, fiducial marker, phase-based measurement, pose estimation, visual servoing

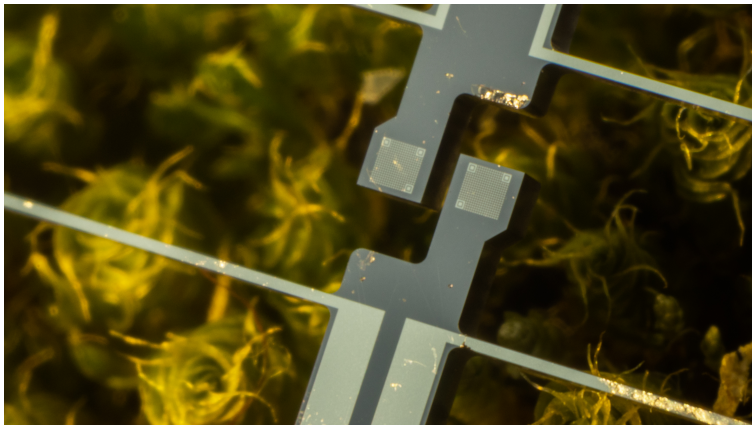

FIG. 1: Picture of two High-Precision fiducial markers, named HP codes in reference to the well-known QR codes, and integrated to a compliant structure dedicated to force-displacement tests.

I. INTRODUCTION

Robots are widespread in all fields of manufacturing and science for their ability to undertake repetitive tasks at high performance levels. Due to the new trend in personalizing products and services, robots are expected to gain versatility. In addition, automating tasks is of key importance for both scientific (repeatable experimental studies required to analyse influential parameters) and manufacturing purposes (scaling-up of the production). As a result, high performances robotics generally necessitates closed loop control, while robots' versatility results from versatile measurements.

In the field of microrobotics, several key results have demonstrated a strong application potential by successfully achieving complex and/or automated tasks such as the insertion of micromechanical components[12], fabrication of fluidic chips[3], soldering of small scale components[4] or assembly of photonic systems[5], micro-optical benches[64] and microelectronic devices[7]. These achievements were made possible by two main approaches, i.e. either by using vision sensors[8910] or force sensors[1112]. They also highlighted the difficulty to quantify the resulting performance especially the relative positioning of components which is a key challenge for characterization, manipulation, motion control and assembly.

Several recent studies addressed this obstacle and have successfully quantified the performances of complex tasks achieved at the microscale: pick-and-place can be realized with micrometer precision using edge detection of the finger tips in 2D[13,14]. Liu et al. have demonstrated the capability to achieve tracking in 3D with a precision of 3 µm[15] useful

for the dexterous manipulation of micro-spheres[16]. Automated assemblies of snap-lock micromechanical structures[17,18,19] and flexible optical components[20,21,22] have been achieved by visual servoing and conducted to a positioning accuracy of 1 µrad and/or 1 mrad.

Very few studies have been able to reach improved performances, typically 0.1 µm, by proposing specific methods and strategies, and without using a scanning electron microscope. Shang et al. combined feedforward control to more regular position controller and force observer for the manipulation of micro-spheres[23]. Chen et al. achieved fiber alignment by telecentric stereo microscopy and associated epipolar and geometry constraints[11]. Li et al. proposed improved template matching-based pose tracking aiming at planar nanopositioning[24]. Bettahar et al. proposed a photo-robotic approach based on active alignment for the 6 DoF (degrees of freedom) robotic calibration and could estimate the positioning accuracy to 50 nm and 70 µrad[25]. These works show the interest in high positioning accuracy in multi-DoF for microrobotics, but appear quite dedicated to applications and/or have very long implementation times.

Vision-based measurement being widely used in microrobotics, it is interesting to note that retrieving high resolution object poses from images acquired through a camera is involved in a lot of applications. Numerous measurement algorithms have been applied at the microscale, namely, corner detection, edge detection, region detection, image correlation, phase correlation, and optical flow methods. Image correlation and phase correlation are the most popular methods due to their ability to provide subpixel resolution. Indeed, nanometer resolution can be typically achieved with regular optical microscopes[26]. However, these methods need the recording of a template image that is then retrieved in the full image. Moreover, the measurement resolution depends on the size and quality of the images (textures, sharpness, etc.).

At the macroscale, many robotic applications rely on fiducial markers placed on the object of interest such as mobile robots[27], augmented reality and collaborative robots[28]. Many markers have been proposed[29], and among them AprilTag[30], ArUco markers[31] and QR codes[32–34] are the most widely used for a large range of applications because of their high versatility. These markers enable storage of binary information and their pose can be retrieved with a single camera. Much research is oriented on the detection time and on reliability[35,36], but very little focuses on subpixel marker detection that is critical for many applications at the microscale.

To address these needs and to overcome the obstacles, this paper presents a novel type of fiducial marker that is based on the design of regular QR codes but embeds a periodic pattern in place of the binary code. Indeed, André et al. recently demonstrated that periodic patterns lead to improved performance with typical subpixel resolutions of one thousandth of a pixel corresponding to nm and µrad measurement resolutions with a 10x microscope[37,38]. The design of the resulting High-Precision markers (named HP codes) is introduced in section II along with the study of influential parameters and the method to efficiently achieve the pose estimation. Section III deals with the experimental investigation of the resulting $XY\Theta$ measurement to quantify the performance of the proposed method. Beyond the disruptive performances reached, the method is calibrated and is expected to provide a high robustness as well as bringing a high versatility through the ease of implementing characteristics. To demonstrate these features, two case-study applications are chosen. The first is introduced in section IV and consists of integrating two HP codes among fluidic chips to enable their automated assembly in the plane through visual servoing with a high positioning accuracy (sub µm is typically required). The second case study is introduced in section V and consists of integrating two HP codes among a mechanical compliant structure resulting in a multi-DoF micro force-displacement sensor. It is applied to the mechanical characterization of single fibers (typical diameter smaller than 100 µm) based on automated microrobotics. It demonstrates the added value of such rich sensory information to achieve the task, but also to analyze the behavior during the test. Section VI ends the paper with the final conclusions and discussions about the work.

Two videos illustrating the results of sections IV and V are provided as supporting information for this paper. A free distribution of the library resulting from section II is available online at `https://projects.femto-st.fr/vernier/`.

II. HIGH-PRECISION FIDUCIAL MARKERS

Retrieving object poses from monocular images is involved in many applications and different fiducial markers have been explored. This section presents the design and the pose estimation process of a new kind of marker derived from QR codes and dedicated to phase-based measurements.

A. Marker design

QR (Quick Response) codes are usually made of several components that can encapsulate digital information in a matrix with entries '0' and '1'. One of these components, called finder patterns[39], allows the in-plane detection of the QR code in a given image. These finder patterns are made of two intricate boxes of '1' and are placed at the corners of the QR code. However, of the four corners available, only three of these finder patterns are placed to ensure an absolute detection in rotation by creating an unambiguous referential. The other components that can be found on regular QR codes such as timing patterns or alignment patterns are replaced by a periodic pattern that will be used for fine subpixelic localization. Fig. 2 presents the design of this new precision fiducial marker, which we named HP code, standing for High-Precision code, in reference to regular QR codes.

The periodic pattern is interpreted as a bidimensional phase matrix with an evolution according to the period of the pattern in the $(-\pi;\pi]$ range. The phase at the center of the HP code is chosen to be set at '0' and is thus placed on a white square. In order to alter as least as possible the phase evolution of the pattern, the finder patterns and the periodic pattern placed at the center of the HP code present appropriate sizes. Therefore, the number of periods used to design an HP code can only be odd, since the center of the pattern has to be a white dot.

In order to identify multiple HP codes in the same image, some dots of the pattern can be removed. With the detection of the presence or absence of these dots, every HP code can be assigned a unique number, thus allowing unequivocal detection of several HP codes on an image. The removal of dots is carried out on the outer border of the HP code in order to minimize phase disturbances on the overall periodic pattern.

B. 2D pose estimation process

The pose estimation of the HP code is performed in two major steps: *(i)* the rough position is detected with the three finder patterns features and *(ii)* the high resolution measure is retrieved from the phase associated to the periodic pattern in both directions. The coarse detection of the HP code position is obtained with an edge detection algorithm as in regular QR codes. This process is able to detect the three finder patterns which specify

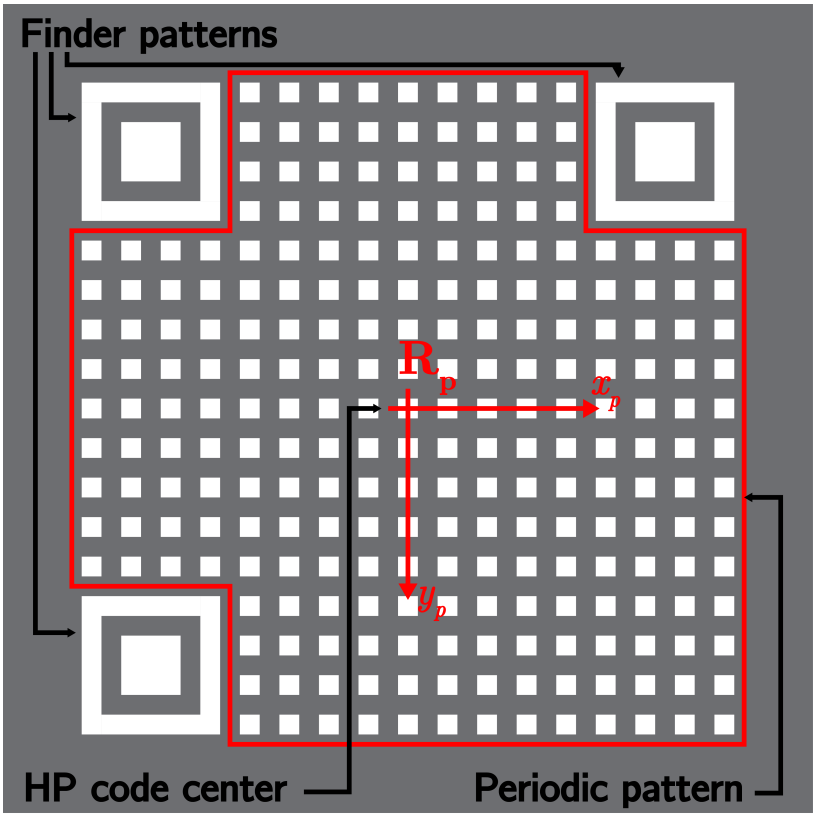

FIG. 2: Design of the High-Precision fiducial marker (HP code) with the three finder patterns and paved with a periodic pattern dedicated to phase measurement.

the overall position and orientation at the center of the HP code. These positions are written respectively x_{rough} and y_{rough}. With such a method, an accuracy of one tenth of a pixel can be achieved.

Once the orientation and center of the HP code have been estimated, a more precise measurement can be made using the bidirectional periodic pattern. This process is done on a sub-image taken around the center computed in the first step with the three finder patterns of the HP code and from which its mean value is subtracted. To retrieve the high accuracy position of the center of the HP code, a method based on the phase distribution associated to the pattern is used. For this, a Fourier transform of the sub-image is performed to detect the main spectral peaks that correspond to the spatial frequencies of the pattern in both directions. To reduce the windowing effects, a Hanning window centered on the HP code position is applied to the sub-image (Fig. 3.b). In accordance with the pattern design, the resulting Fourier spectrum (Fig. 3.c) is made of six main lobes, each one being the phase

conjugate of its symmetrical one with respect to the central DC coordinates. Spectral peak f_1 is representative for one principal direction of the periodic pattern whereas peak f_2 is representative for the perpendicular direction. Corner peaks of higher spatial frequencies are not considered. They represent diagonal orientations at $\pm\pi/4$ of the main pattern directions. The remaining secondary peaks with lower magnitude and distributed on a regular grid correspond to harmonic frequencies and are not considered neither. In the Fourier domain, the pattern directions are clearly separated, as represented by peaks of interest f_1 and f_2, allowing the independent and parallel processing of both directions. For that purpose, spectral peaks f_1 and f_2 are isolated through the application of a bandpass filter made of a 2D Gaussian curve. Then, two successive inverse Fourier transforms, applied to the obtained single-peak filtered spectra, extract the signals associated to both directions respectively. Since the complex conjugate of peaks f_1 and f_2 were discarded, the results of these Fourier transforms are complex with their angle representative of the spatial distribution of the pattern stripes, as represented in Figs. $3.d_1$ and $3.d_2$. Indeed the white centers of dots correspond to a wrapped phase of 0 rad whereas the black middles between dots correspond to a wrapped phase of $\pm\pi$ rad. More details on this phase processing can be found in[37,38].

The goal of this process is to retrieve the pattern center beyond the pixelic discretization of the image by means of the phase associated to the periodic character of the HP code. Since the dot distribution is regular, after unwrapping, the phase maps $\phi_1(x, y)$ and $\phi_2(x, y)$ are linear and can be fitted by a least square plane for better noise rejection. The resulting equations (Eq. 1) encode the HP code position with a high subpixelic resolution. However, constant c_1 and c_2 are obtained with a $2k\,\pi$ uncertainty that is removed from the previous determination of the coarse pattern position. Eventually, the correct and high resolution center of the HP code is determined by adjusting Eq. 1 as described by inequality 2.

$$\begin{cases} \phi_1(x, y) = a_1 x + b_1 y + c_1 \\ \phi_2(x, y) = a_2 x + b_2 y + c_2 \end{cases} \tag{1}$$

$$\begin{cases} -\pi < a_1 x_{rough} + b_1 y_{rough} + c_1 + 2k_1\pi < \pi \\ -\pi < a_2 x_{rough} + b_2 y_{rough} + c_2 + 2k_2\pi < \pi \end{cases} \tag{2}$$

with k_1 and k_2 being integers. This continuous phase distribution unlocks the spatial sampling of the image and, once each least-square plane computed, the coordinates $x_{pattern}$ and $y_{pattern}$ of the periodic pattern center are given by Eq. 3.

$$\begin{cases} x_{pattern} = \frac{b_1 c'_2 - c'_1 b_2}{a_1 b_2 - a_2 b_1} \\ \\ y_{pattern} = \frac{a_2 c'_1 - a_1 c'_2}{a_1 b_2 - a_2 b_1} \end{cases} \tag{3}$$

with $c'_1 = c_1 + 2k_1\pi$ and $c'_2 = c_2 + 2k_2\pi$.

As this result is in pixel, the scale factor s needs to be computed to retrieve a physical measurement. Since the physical period λ_{mm} of the HP code pattern is known, s can be calculated knowing the pixelic period λ_{px} of the pattern in the image as derived from the slope of the phase plane equations by Eq. 5.

$$s = \lambda_{mm} \ / \ \lambda_{px} \tag{4}$$

with

$$\lambda_{px} = \frac{2\pi}{\sqrt{{a_1}^2 + {b_1}^2}} \tag{5}$$

The scaled position of the center of the HP code is therefore the product of the pixel size Eq. 4 by the already known positions in pixel $(x_{pattern},\ y_{pattern})$.

Finally, the phase planes allow us also to retrieve the angle θ of the HP code:

$$\theta = \text{atan2}\,(b_1, a_1) \tag{6}$$

III. PERFORMANCE OF THE MEASUREMENT

A. HP code sizing

Since the presented method is based on the analysis of the Fourier transform applied to the HP code image, the number of periods appearing on the image affects the position accuracy. In order to search for the optimal number of periods to use (in the printing of the HP codes), simulations have been performed to study the impact of the number of periods on measurement accuracy. For each studied number of periods, a set of 100 synthesized images is generated with the HP code at random positions. Then, the standard deviation (STD) of the error between the reference position and the estimated position is computed, and the results shown in the graph of Fig. 4. The same simulations are conducted with images generated with a quantification on 4096 levels (12 bits) corresponding to quality image sensors and with an additive white noise of a magnitude of 650.

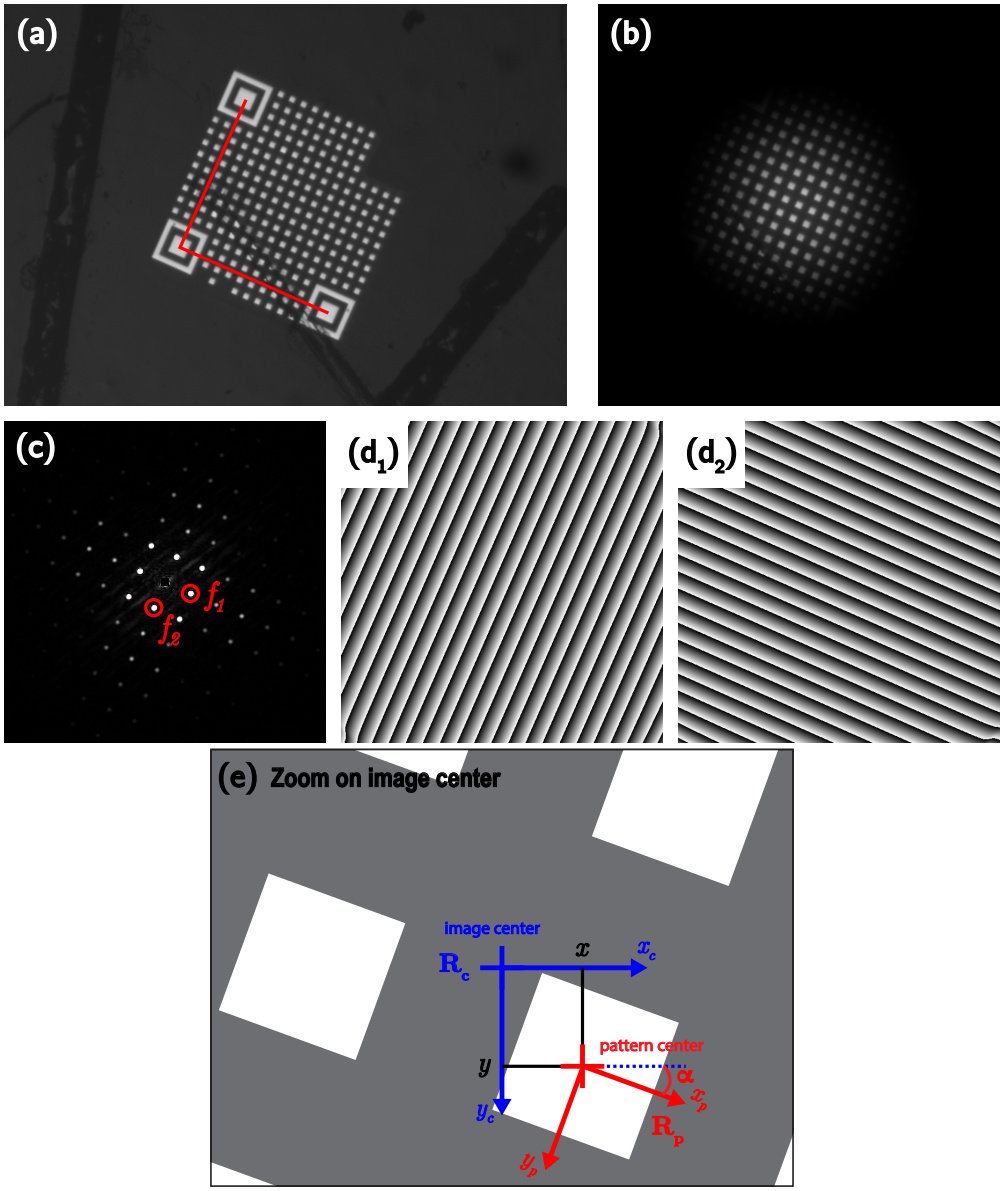

FIG. 3: Major steps of the phase-based position measurement: (a) HP code as acquired by the camera; (b) sub-image taken at the center of the HP code with a Hanning window; (c) Fourier spectrum exhibiting the two peaks f_1 and f_2; (d_1) and (d_2) show the inverse Fourier transform after bandpass filtering of each of the peaks; and (e) highlights the shift presented in Eq. 3 between the rough center of the HP code and the phase-based center.

Simulation results show that even with a low number of periods contained in an HP code pattern, a subpixelic position accuracy can be achieved below 0.01 pixel. As expected, as the number of periods grows the accuracy further improves and stabilizes at below one thousandth of a pixel beyond 17 periods. In the rotation analysis, the results track with

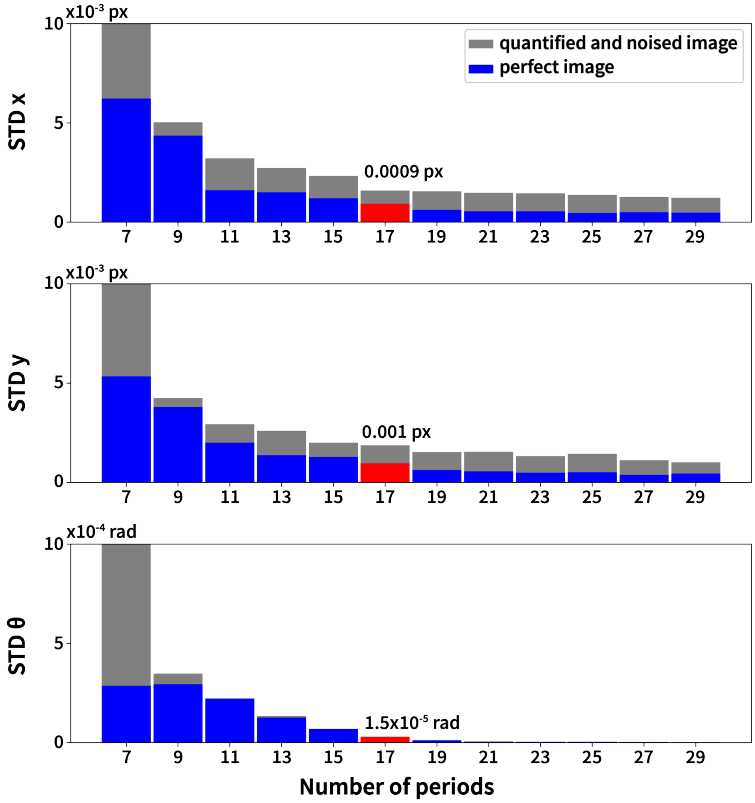

FIG. 4: Evolution of the standard deviation of the position and orientation errors computed on 100 frames for different numbers of periods contained in the HP code. Both perfect and noised images are simulated and highlighted respectively in blue and gray.

results obtained for x and y. When the number of periods is equal to or greater than 17 periods, a resolution of 10^{-5} rad is achieved.

In the case of quantified and noised images, the errors decrease only slightly beyond 17 periods. Therefore, the retained number of periods to design the HP code is 17, as highlighted in red in Fig. 4.

B. Experimental performance with one marker

Several experiments have been carried out to study the performance of the method in a real case. HP codes with 17 periods of 40 µm have been realized on a glass wafer by photolithography in a clean room and observed by means of an inverted microscope (Olympus IX73) equipped with a 5× objective (Optem M Plan Apo). The images of the HP codes are recorded with a CMOS camera (IDS UI-3280CP-M) with a 3.45 µm pixel size. The camera

is set at 20 frames per second encoded on 12 bits (thus allowing a range of 4096 gray values). A rotation stage (Smaract SR-2013) with a closed loop resolution of $4.4 \cdot 10^{-7}$ rad and a range of 2π, and a translation stage (Nano-MET10 from MadCity Labs) with an internal resolution of 0.01 nm and a range of 10 µm are used. Finally, the whole experimental setup is placed on an anti-vibration table in a temperature-controlled room.

1. Comparison to other position measurement methods

To ensure that the presented method provides better results than other classical computer vision algorithms, a first comparative test is performed. The phase-based method presented in this paper is confronted with two usual methods. The first one applies feature detection to the finder patterns and deduces the HP code center from the location identified for these three markers. This method relies on edge detection and corresponds to the method commonly used for regular QR code detection[40]. The second one determines the set of pixels belonging to the whole HP code and then calculate the corresponding image moment to determine the centroid associated[41]. For these experiments, the HP code and the camera were disposed in such a way that the motion operated by the 1D translator is aligned with both the lines of the image sensor and the first direction of the HP code. Images acquired in this way are then processed with the three different methods compared and, among the x, y, θ data reconstructed, only the x coordinate of the HP code center is considered to compare the performances of the different algorithms.

Fig. 5 presents the evolution of the detected x coordinate of the HP code as retrieved from the set of images recorded while steps of 50 nm at a 0.5 Hz rate are sent to the translation stage where the HP code is affixed. The magnitude of noise observed in this figure is thus representative of the small motion detection capabilities of the three compared methods respectively. Edge detection method applied to the three finder patterns shows a resolution around 50 nm, that is just below $1/10^{th}$ of a pixel. The centroid method based on pattern moment is slightly more resolute and detects steps down to 25 nm. This improvement is consistent with the fact that the amount of information considered is extended to the whole set of pixels belonging to the pattern. Finally, the phase-based method presented in this article clearly shows a leap in terms of resolution power since the square signal is finely retrieved. The next sections study in more details the performance of the method in terms

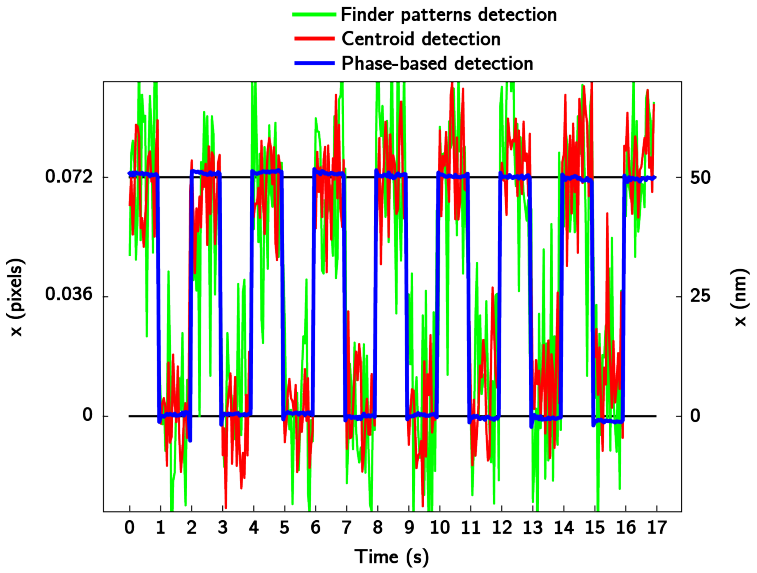

FIG. 5: Comparison of the position obtained for a 50 nm square signal set at 0.5 Hz. Three methods are presented: in green the center is retrieved from the three finder patterns of the HP code, in red the centroid of the center is computed with the moment of the pixels of the pattern, and in blue the phase-based method proposed in this paper is used.

TABLE I: Experimental STD (made out of 100 images) and linearity error.

Axis	Static noise (std)	Linearity error
x	1.8 nm	0.09%
y	2.4 nm	not tested
θ	$4.56 \cdot 10^{-6}$ rad.	0.005%

of static noise, resolution and linearity.

2. Static test

The first experiment studies the noise level when nothing is moving in the setup. This static noise measurement allows the determination of the best achievable resolution. To carry out this experiment, 100 images of the HP code are taken under the microscope without any movement involved. As shown in Table I, under static conditions, the measure presents a noise of around 2 nm along the x and y axes, and a static noise of around 5 µrad in rotation. Therefore, this test shows the level of noise of the setup with the stage off.

3. Linearity test

A test of linearity is conducted to ensure that the method allows a uniform position accuracy both in translation and rotation. To perform this experiment, a first set of images is acquired at the camera frame rate while the translation stage moves with the HP code attached to it and along its working distance of 10 µm. A similar test is conducted with the HP code fixed on the rotation stage while moving about a 2π range. The measures from the HP code are then compared with the values of stage sensors to calculate the linearity. The results of this experiment are shown in the second column of Table I and present a linearity error below 0.1% in both translation and rotation. The linearity test demonstrates that the method can be trusted with a high accuracy over the whole range of used actuators.

4. Resolution test

The last experiment with the HP code tackles the resolution of the measure that can be achieved. The measurement resolution is defined as the smallest variation of distance detected by the measurement system. Experimental conditions for the resolution measure are the same as for the linearity test except that the translation stage is set with a 5 nm square signal and the rotation stage is set with a 10 µrad square signal, both with a fixed frequency of 0.5 Hz to have 20 frames acquired on each step of the signal. Results show that in these conditions, both square signals can be measured as presented in Fig. 6. By drawing the mean values on each step, and the error bars corresponding to the standard deviation of the static noise presented in Section III B 2, the recovery of the square signal can be seen with more ease. Therefore, this test confirms that the resolution capability of the method is below 5 nm in position and 10 µrad in rotation, and limited by the static noise level, i.e. 2 nm and 5 µrad.

Note that the high performance level of the method relies on the periodic frame in the internal part of the HP code. The finder patterns used for preliminary coarse measurement are not critical and different features could have been chosen successfully. However, our choice of QR-like finder patterns allows the re-use of fast and well-proofed algorithms and software already available.

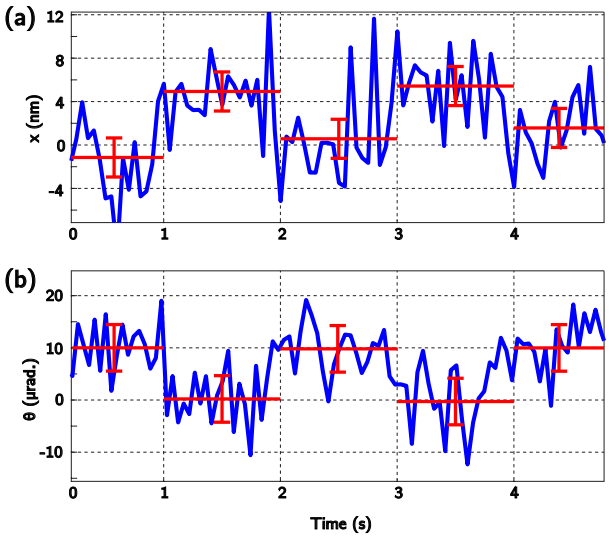

FIG. 6: Resolution tests with 5 nm height squares input signal for the translation and 10 µrad for the rotation. Horizontal red lines represent the mean value of each step (20 images each) and vertical bars represent the standard deviation of the static noise studied in Section III B 2.

IV. APPLICATION TO MICROFLUIDIC CHIP ASSEMBLY

To demonstrate the potential of this approach combining high-precision and versatile $XY\Theta$ measurement, HP codes are used for a key microrobotic application that consists of the automated assembly of two fluidic chips. Indeed, these last years, lab-on-chip devices performing cellular analysis and sorting have gained wide attention[42],[43]. These devices are composed of fluidic channels to ensure fast and long range displacements of the cells, but also actuators and/or sensors, such as electrodes, to generate acoustic or electric fields to precisely control the position of the cells in the area of interest. To ensure a precise positioning of the cells, the position of the electrodes with respect to the fluidic channels must be set accurately [44], requiring high levels of precision in the assembly of the chip. However, the fabrication of these chips is still a challenge. Indeed, they are composed of two glass wafers on which resin channels and metallic electrodes have been accurately deposited by microfabrication techniques to form the bottom and top parts of the chips. These two wafers must then be assembled so that the channels and electrodes are accurately aligned with a positioning accuracy less than 1 µm and 1 mrad. Fig. 7.(a) highlights this case study, which is a typical microfluidic chip. The cross views of chips appear as described in Fig. 7.(b).

To reduce fabrication costs, several chips are fabricated on the same wafer. They are

separated by saw dicing at the end of the fabrication process. The assembly of the two glass plates cannot be done directly at the wafer level because when separating each chip, residual stresses are released, breaking the chips. The assembly must then be carried out at the chip level, after saw dicing. However, the cutting of these elements is not precise enough to be used as a reference. We thus propose to use a robotic system to position the chips and align them. This system must be able to move them along 3-DoF in a plane parallel to the glass plates. The robotic system is used to position the glass chips, so that the top and bottom fluidic channels and electrodes are correctly aligned. The bonding of the top glass plate with the channels is performed according to fabrication techniques described in the literature[45]: the microfluidic circuit, made of SU8 resin, is insulated to fix the assembly.

A. Assembly system

The assembly system (Fig. 8.(a)) consists of a 6 DoF precision robot handling the upper holder glass plate held by micro-suction pads, a fixed support holding the lower plate in position also by vacuum and an optical microscope observing through both glass plates from the top, giving images of the chip such as the ones shown in Fig. 8.(b). The lighting is provided by red LEDs positioned on the robot side support. The robot consists of 6 axes arranged along a PPPRRR serial kinematic structure. The axes are driven by stick-slip piezoelectric actuators from Smaract Company. The robot can perform movements in the 6 DoF of the operational space with a resolution of one nanometer and a few microdegrees. The positioning of the glass plates is controlled in velocity by visual servoing. In this application, only 3 DoF are sufficient, the 6 DoF are used only for the loading phase of the glass plates before the assembly and for storage after assembly.

B. Visual servoing

The objective of this task is to achieve the relative positioning of the two fluidic chips in the plane ($XY\Theta$) through visual servoing using the HP codes, with a positioning accuracy typically better than 1 µm and 1 mrad. The vision system has a spatial resolution of 2 µm/pixel (typical case), which is not sufficient to obtain the required positioning accuracy for the assembly task using feature-based methods. The solution chosen was therefore to

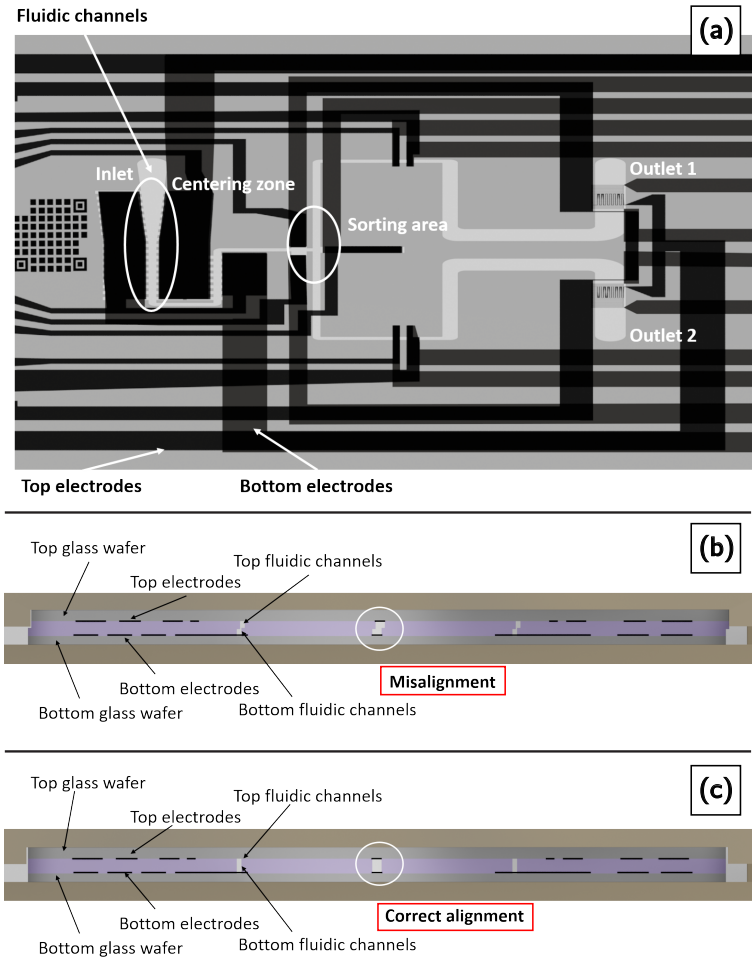

FIG. 7: Layout of the assembled fluidic chips. (a) Top view. The cells are injected in the inlet hole, centered by electrodes in the centering area, and sorted towards one of the two outlets. (b) and (c) Cross view of the chip assembly. The top and the bottom glass plates must be correctly positioned to ensure a proper alignment of the electrodes and fluidic channels (sketch not to scale).

print, by gold deposition, HP code markers on each glass plate to accurately measure their relative positions. As these HP codes are deposited during the same fabrication step as the electrodes, the accuracy of their positioning with respect to the fluidic channels and the electrodes is given by the accuracy of the mask generator (Heidelberg DWL200), which is calibrated several times a year.

The alignment of the glass plates then relies on the relative position of the HP codes. Since the position of both codes is measured simultaneously, their relative position, and therefore the relative position of both fluidic chips, can be estimated accurately. The left HP code in Fig. 8 placed on the lower plate is used as a reference. The relative desired

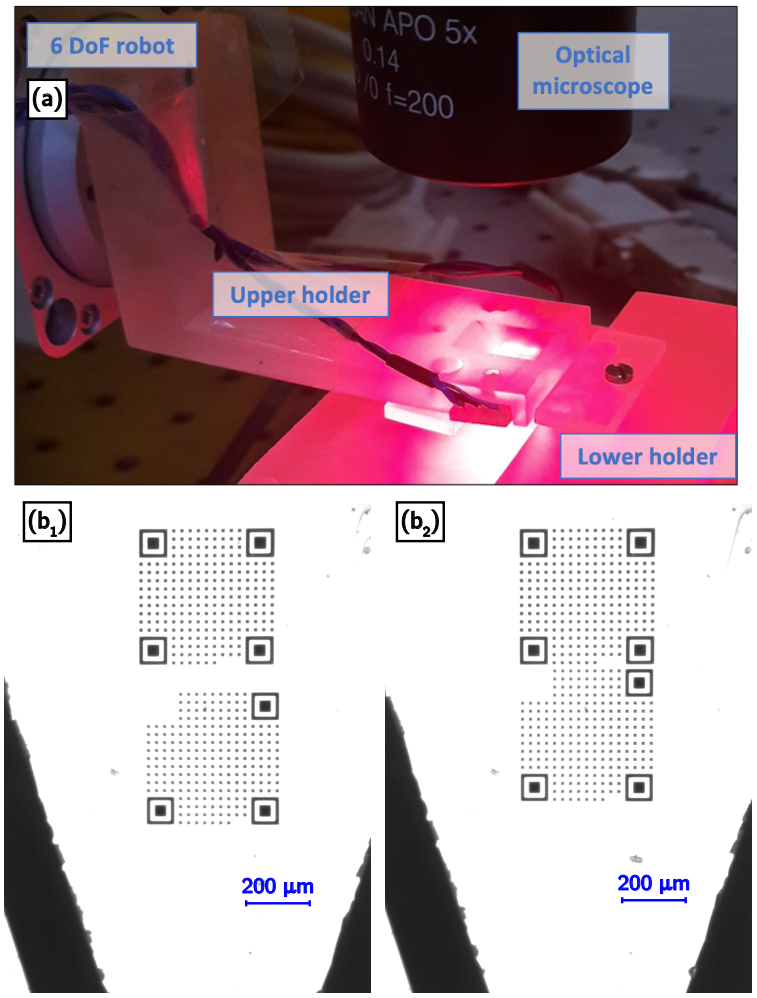

FIG. 8: Experimental setup for the assembly of microfluidic chips. (a) Close view of the experimental setup. (b_1) and (b_2) Images of the HP codes before and after the visual servoing. The left HP code is part of the lower plate of the fluidic chip, while the right HP code is part of the upper one.

position of the right HP code (on the upper plate) is 680 µm (corresponding to 17 entire periods) in the x direction, 0 in the y direction, and 0 in orientation.

To control the robot, we followed the classical visual servoing scheme proposed in Ref.[46] and presented in Fig. 9.(a). The relative position errors $\mathbf{e}$ (which is zero in case of a perfect assembly) is defined by:

$$\mathbf{e} = \mathbf{x}_2 - \mathbf{x}_1 - \mathbf{d} \tag{7}$$

where $\mathbf{x}_1 = (x_1, y_1, \theta_1)$ and $\mathbf{x}_2 = (x_2, y_2, \theta_2)$ are the 2D poses of both HP codes, and $\mathbf{d}$ is the desired distance between the HP codes.

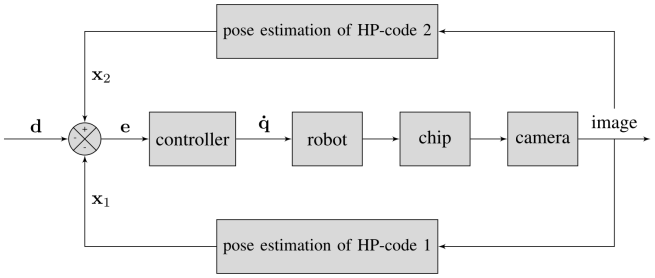

(a) Visual servoing

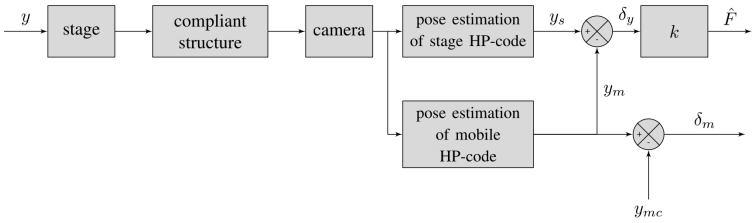

(b) Force-displacement measurement

FIG. 9: Block diagrams of the assembly task and of the force-displacement sensor.

Then, the end-effector velocities are given by:

$$\begin{bmatrix} \mathbf{v} \\ \boldsymbol{\omega} \end{bmatrix} = -\gamma \mathbf{L}_e^{+} \mathbf{e} \tag{8}$$

with $\mathbf{L}_e^{+}$ the pseudo-inverse of the interaction matrix and γ a proportional coefficient.

Finally, the joint speeds are calculated using the robot Jacobian matrix $\mathbf{J}(\mathbf{q})$, such as:

$$\dot{\mathbf{q}} = \mathbf{J}^{-1}(\mathbf{q}) \begin{bmatrix} \mathbf{v} \\ \boldsymbol{\omega} \end{bmatrix} \tag{9}$$

This scheme makes the position errors decrease exponentially and behave like a first order decoupled system.

C. Assembly results

The experimental investigations aim to quantify the performance obtained by the robotized assembly of fluidic chips based on visual servoing. In the first tested scenario, the position of the left HP code is only measured once at the beginning of the servoing. Indeed, the left marker is placed on the lower plate which is not supposed to move. The position and the orientation to reach is then calculated relative to the left marker. Unfortunately,

this method was not successful. Persistent measurement noises in the angular measurement of the right marker results in too large positioning error during the visual servoing. The measurement noises are due to parasitic displacements of the stand of the microscope and of the robot. To cancel these vibrations, the relative position of both markers can be measured in each image. In this way, the relative movements between the microscope and the robot do not add noise to the measurement.

Two results of the visual servoing are presented in Fig. 10 for different initial conditions corresponding to the left HP code that is initially roughly positioned using the manipulator sensors. In both cases, the servoing shows a fast convergence phase followed by a longer one leading to a fine alignment and rejecting all disturbances.

In Fig. 10.(a), the position errors drop below 50 nm at time $t = 111$ s. Between $t = 111$ and $t = 120$ s, the standard deviations of absolute errors $|\mathbf{e}_x|$, $|\mathbf{e}_y|$, $|\mathbf{e}_\theta|$ are, respectively, 20.1 nm, 14.9 nm, and 17.5 mdeg (0.31 mrad).

In the second experiment (Fig. 10.(b)), the position errors drop below 50 nm at time $t = 131$ s. Between $t = 131$ and $t = 140$ s, the standard deviations of absolute errors $|\mathbf{e}_x|$, $|\mathbf{e}_y|$, $|\mathbf{e}_\theta|$ are, respectively, 10.8 nm, 18.0 nm, and 17.9 mdeg (0.31 mrad).

These experimental results show the capability to successfully achieve the assembly of planar fluidic chips with a positioning accuracy below 50 nm in position and below 1 mrad in orientation.

V. APPLICATION TO A FORCE-DISPLACEMENT SENSOR FOR SINGLE FIBER COMPRESSION

A second application, also of key interest in microrobotics, that is chosen as a case study in this paper deals with the simultaneous force and displacement sensing resulting from the integration of two HP codes on a compliant structure. Indeed, force sensing has always been a key issue for micro and nanoscale applications. More particularly, sensing force ranging from a few mN to some hundreds of mN is of key interest to achieve manipulation, assembly and characterization tasks in many application fields (biology, material science, manufacturing, medical applications, and so on). Despite these huge needs, very few sensors have been developed and/or transferred for commercial use due to many technical and physical limitations[47484950]. Micro-force sensors are always made of a compliant, mechanical,

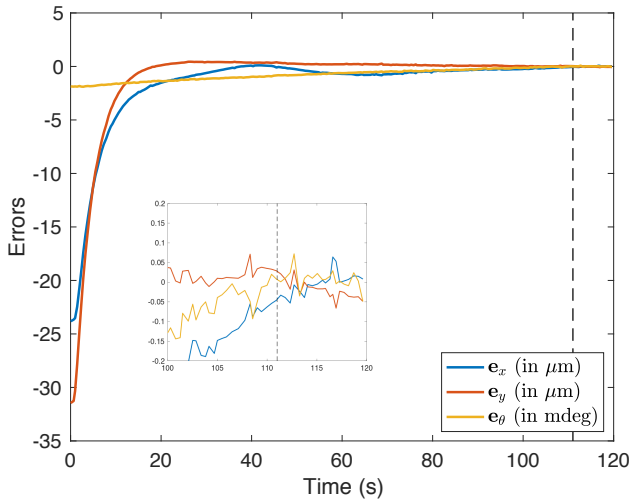

(a)Assembly #1

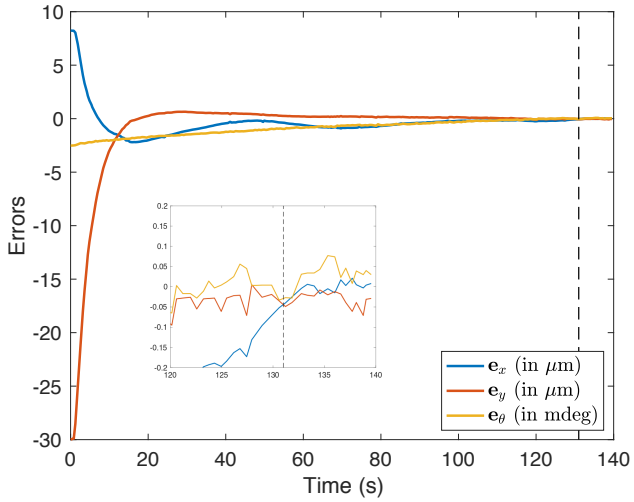

(b)Assembly #2

FIG. 10: Evolution of the position and orientation errors during visual servoing after coarse positioning (as in Fig. 10.(a)) for two chip assemblies.

passive structure associated with a device able to measure a displacement, strain or resistance change, among other quantities. Force is never a direct measurement but calculated by measuring one of the aforementioned quantities, and feeding the results into an established physics model. For these reasons, the accurate identification of the model's parameters, through a calibration process, is of key interest, same as quantifying performances such as the linearity and trueness. In addition to the interest of force sensing, simultaneously achieving force and displacement sensing appears even more appealing. For these reasons, we propose to study in this section the integration of the HP codes proposed in this paper with

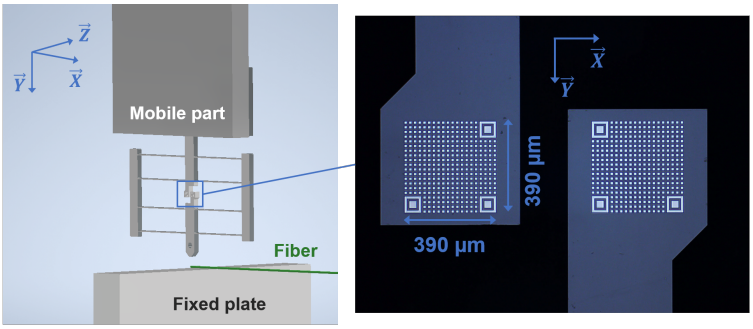

FIG. 11: Force-displacement sensor made of a CT joint compliant structure and including two HP codes.

a compliant structure that will be used as a force-displacement sensor for the mechanical characterization of single fibers through transverse compression tests.

A. Force-displacement sensor

The proposed force-displacement sensor is a compliant structure that includes 8 bending beams organized along a CT joint (Compliant Translation joint [51]) configuration (Fig. 11). This configuration enables highly straight motion of the mobile part of the sensor (that will be in contact with the object to be characterized) and the part of the sensor that is fixed to the robot. Two HP codes are added through photolithography and metal deposition onto the mobile and fixed parts of the sensor. When an external force is applied to the sensor, a relative motion between these two codes occurs along the y direction. An external camera provides images such as in Fig. 11-left and the phase-based position estimation process presented in previous sections enables us to accurately estimate this relative motion along the main direction of the motion (y axis) but also out of the main direction of the motion (x axis) including potential relative rotations (θ angle around the z axis). These out of the main direction measurements are of key interest for mechanical characterization purposes. Indeed, they give key information about the behavior of the sensor during the test that is related to highly influential parameters. The presence of couplings, errors in the initial alignment of the sensor to the fiber, and parallelism errors between the substrate and the tip of the force-displacement sensor are typical examples.

The external force applied to the sensor along the y axis can then be estimated by:

$$\hat{F} = k.\delta_y \tag{10}$$

where $\hat{F}$ is the estimated force, k the stiffness of the sensor along y and δ_y the relative displacement along the y axis measured by vision. The stiffness of the force sensor directly depends on the dimensions of its 8 constitutive beams, such as:

$$k = 2.\frac{E.w.t^3}{L^3} \tag{11}$$

where E is the Young's modulus of the material used, t the thickness of the beams (dimension in the same direction as the applied force), w is the width and L the length of the beams. The sensor used in this study has been designed for the purpose of single fiber characterization (experimentation given in the next paragraph). To meet the corresponding specifications, the force sensor has been made of silicon through clean room fabrication with the following beam dimensions: $t = 100$ µm, $w = 500$ µm and $L = 6$ mm. Estimating the Young's modulus of silicon at $E = 169$ GPa corresponds to a theoretical stiffness of $k = 782$ N/m.

Since the sensor's operating principle relies on displacement tracking, it can be used as a force and displacement sensor simultaneously, as explained in Fig. 9.(b). This is particularly useful for compression test applications, where the sensor gets directly in contact and compresses a deformable object. While the force is measured through the relative motion between the HP codes, the displacement of the object during compression can be obtained directly from the mobile part of the sensor by:

$$\delta_m = y_m - y_{mc} \tag{12}$$

where δ_m is the relative displacement of the object during compression, y_m is the y coordinate of the HP code on the sensor's mobile part and y_{mc} is the y coordinate of the same HP code when the sensor-object contact is first established (when a relative motion between both HP codes appears).

B. Experimental setup

An experimental setup was developed for two complementary purposes: (i) carrying out transverse compression tests on single synthetic or plant fibers, and (ii) performing

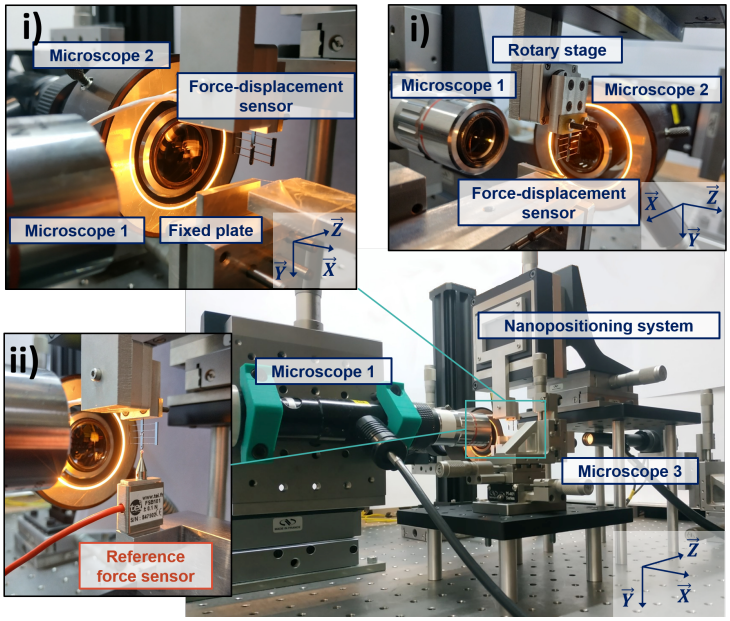

FIG. 12: Experimental setup in: (i) fiber characterization configuration, (ii) sensor calibration configuration.

calibration (sensor stiffness identification) by compressing a reference force sensor (Fig. 12). In both cases, the proposed force-displacement sensor is directly compressing its target. It is mounted on a 5 DoF micropositioning system to accurately position and orient its tip relative to the compressed object. This system consists of a XYZ manual micropositioner, a nanopositioning stage (PI PIHERA 629.1) used to lower the sensor along the y axis and compress its target and, finally, a rotary actuator (SmartAct SR-2013) to control the relative angle between the sensor and the target. In the case of a fiber compression test, the sample is positioned on a fixed substrate in a free-clamped configuration, with the free end directly under the sensor tip. In the case of a calibration test, the reference force sensor (TEI FSB101) is mounted on a rigid support, facing the sensor. Microscope 1 enables us to visualize the relative motion between both HP codes during the compression test. The vision algorithm presented in section II is used to accurately estimate the position of the HP codes. Thus, the applied force and the displacement of the compressed object can be acquired. Potential coupling motions can also be measured. Microscope 2 is used to visualize the cross-section of the fiber during the test, while Microscope 3 gives a view of the fiber along its length (Fig. 13).

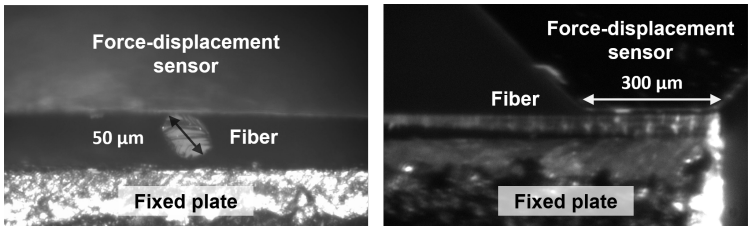

FIG. 13: Polyamide 11 fiber during compression tests along: cross section (left), length (right).

C. Experimental investigations

1. Calibration tests

During calibration tests, the relative motion δ_y of the HP codes and the force signal from the reference force sensor F_{ref} are acquired. The stiffness k of the force-displacement sensor is estimated through linear regression by assuming that $F_{ref} = k.\delta_y$. Three force-displacement sensors were calibrated by compressing the reference force sensor 20 consecutive times. A mean stiffness of $k = 667 \pm 1$ N/m (standard deviation value) was identified across all tests. This corresponds to a 14.7% difference with the estimated stiffness. Considering that a 5% variation of the beam's thickness leads to a 14% change in stiffness, the difference between theoretical and experimental values is acceptable, especially once the uncertainty of all geometric and material parameters is considered. The average difference during the whole calibration test between the force measured by the force-displacement sensor and the reference sensor is 0.27 mN or 0.2% of the reference sensor's used measurement range (200 mN). This small difference can be accounted for by noise, slight misalignment between sensors and slippage at the contact surfaces. To compare the performance of the two sensors, the force measurement noise at a constant force level is averaged across all tests. The reference sensor noise is 0.27 mN, or 0.09% of its measurement range. The force-displacement sensor has a noise of 0.04 mN, or 0.01% of the measurement range, calculated for each sensor by multiplying its stiffness by the maximum relative displacement between the HP codes (500 µm). The noise level of the reference sensor is thus almost ten times higher than the HP codes measurement noise, when they are compared to their respective measurement ranges. In other words, the HP codes allow force measurements over a wider range while offering higher precision.

2. Rigid support tests

In order to better understand the sensor's behavior and quantify its performance, tests against a rigid support were performed to eliminate, at first, the influence of a deformable object. To assess the repeatability of the sensor's behavior, tests were repeated ten times. Fig. 14 shows the evolution of the three coordinates (y, x, θ) obtained from the HP code tracking, as a function of time. The mean evolution over the ten tests is plotted. In the y direction both HP codes follow the same trajectory until a contact is established. The mobile code is then stopped, since it is pushing against a rigid support. The sensor's beams are bending allowing the fixed code to continue its trajectory. The HP codes follow the same trajectory once again once the contact is lost. A similar behavior occurs on the x axis, with a much smaller magnitude of displacement, while the rotation behavior is slightly different. The fixed HP code rotation can be attributed to a nonlinear displacement of the actuator that does not produce a perfectly straight movement. For the mobile code, the rigid support stops the rotation when the contact is established. To quantify the repeatability, the standard deviation between tests of y, x and θ quantities is calculated at each time step and averaged for both HP codes, resulting in: 41 nm in the y direction, 111 nm in the x direction and 69 µrad for the rotation θ. Contrary to y and θ, the deviation in x is much more important since sliding and torsion during the contact steps is hardly predictable and repeatable at the microscale.

3. Single fiber compression

In this section the compression test of a single polyamide 11 (PA11) fiber, with a diameter of 50 µm, is presented. The sample is mounted as shown in Fig. 12 and the force-displacement sensor is coarsely positioned manually at first. Quite often, electrostatic forces cause the fiber to adhere to the tip of the sensor. The sensor and fiber are then lowered against the fixed lower plate using the nanopositioner. The applied force is measured through the fiducial markers with Eq. 10 and the fiber's displacement with Eq. 12. The force-displacement curve as well as the evolution as a function of time is given in Fig. 15. Three distinct steps can be observed from the force-displacement curves. In the free motion step, the fiber is stuck to the sensor and follows its movement showing no resistance, slightly fluctuating around zero.

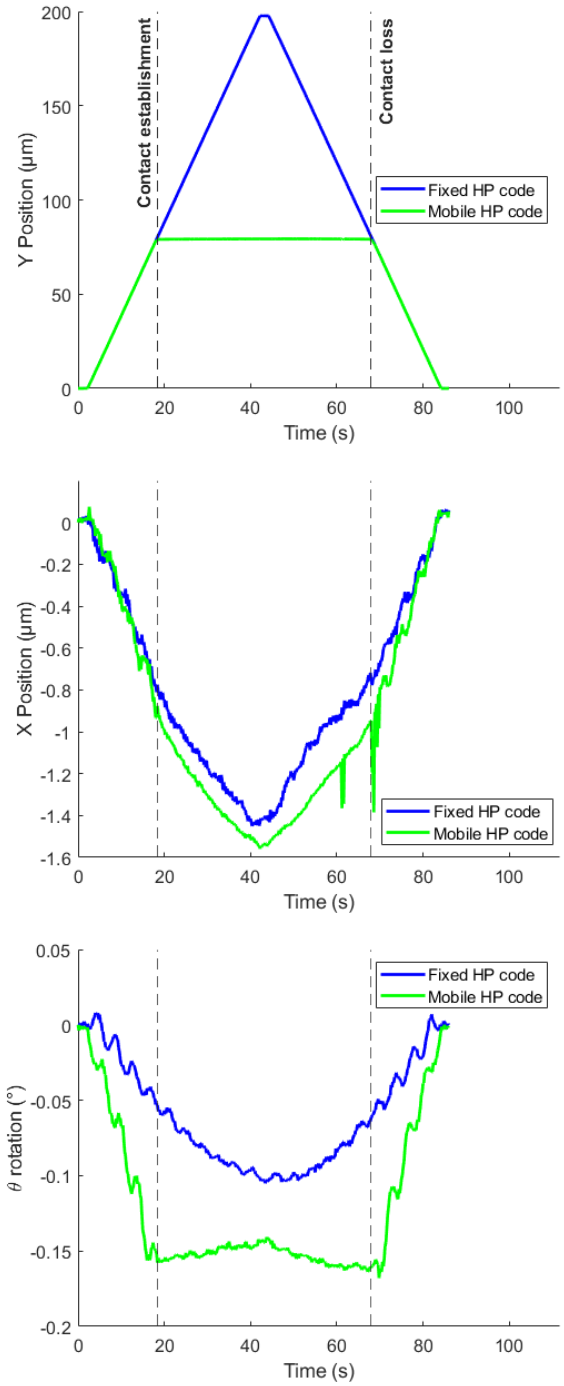

FIG. 14: Mean HP code measurements over 10 tests against a rigid support: Y, X and θ.

During the rigid body movement step, the fiber gets in contact with the lower plate and starts rotating and sliding until it becomes completely trapped between the sensor and the lower plate. This behavior results in the gradual nonlinear increase of the compression force. During the third step, the rigid body motion has been completely established and the fiber

is being compressed. The force increases rapidly in a close to linear relation with the fiber's displacement. During this step, the force displacement data can be fed in a mechanical model in order to identify the fiber's material properties.

These results demonstrate several key achievements. The first one lies in the high quality of the curves that enables us to quantify some key mechanical parameters of the fibers such as the transverse stiffness which is a parameter of key interest but highly difficult to estimate with other regular methods. The second key achievement relies on the very fine understanding of the overall behavior of the fiber but also of the sensor during the tests, which leads to a to clear identification of several key phenomena. Overall, these experiments demonstrate the major application potential of HP codes inserted onto a compliant structure. They offer simultaneous force and $XY\Theta$ displacement sensing with disruptive range to resolution ratio, and can be easily implemented in microrobotic platforms.

VI. CONCLUSION

In this paper, High-Precision fiducial markers, called HP codes, have been proposed to easily automate microrobotic tasks requiring accurate and $XY\Theta$ measurements. Their design consists in merging regular QR codes and periodic patterns to enable phase-based measurements. The method to precisely locate an HP code in an image has been detailed and connects to a set of characteristics of key importance: high resolution (one thousandth of a pixel) can be achieved in a highly versatile, calibrated and robust way. Several experimental studies have been conducted to quantify several key performance characteristics, but also to demonstrate the wide potential of the approach. Firstly, the vision tracking of one HP code aiming at microrobotic applications demonstrated high resolution, i.e. 2 nm in translation and 5 µrad in rotation. Secondly, two HP codes have been printed onto micro-fluidic chips enabling their automated assembly through visual servoing with a positioning error below 50 nm and 1 mrad. Thirdly, two HP codes have been printed onto a compliant structure to enable simultaneous force-displacement sensing. This sensor has been used experimentally to achieve automated compression tests of single fibers bringing very rich information that typically enables us to understand, in depth, the behavior of the fiber during the tests. All these results demonstrate the versatility of the proposed approach because they show that it can be easily implemented in several very different applications. The performance

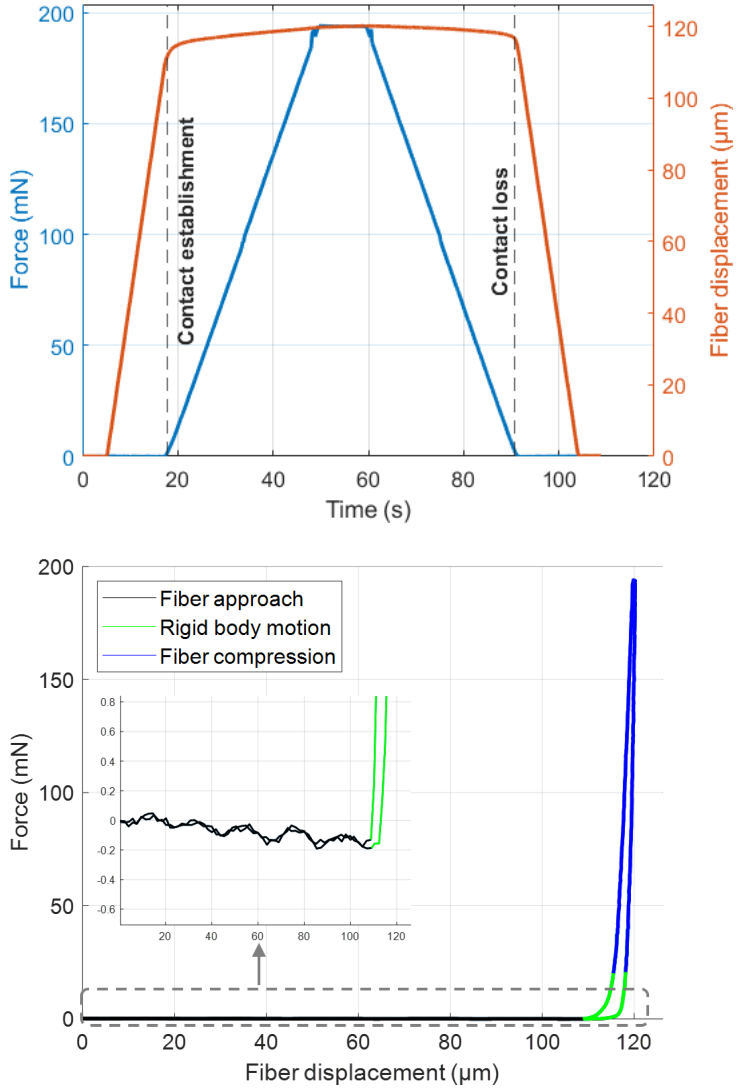

FIG. 15: Transverse compression test of a PA11 fiber at 10 µ/s: applied force over a length of 300 µm and fiber displacement.

(very high resolution) but also the possibility to integrate one or several HP codes for position, displacement and/or force measurement along several DoF ($XY\Theta$) are also key characteristics of the method. These make the proposed HP codes a particularly relevant approach for many applications such as the tracking of components (possibly a part of a microrobot for closed loop control or for characterization), the manipulation, the assembly and the mechanical characterization of samples that all are of high impact for the near future.

Acknowledgment

These works have been partially funded by the Bourgogne Franche-Comté région, by the COLAMIR project (contract ANR-16-CE10-0009), by the MiMedi project funded by BPI France (grant No. DOS0060162/00) and the European Union through the European Regional Development Fund of the Region Bourgogne-Franche-Comte (grant No. FC0013440), and supported by the EIPHI Graduate school (contract ANR-17-EURE-0002), the French ROBOTEX network (grant no. EQUIPEX+ TIRREX ANR-21-ESRE-0015) and the French RENATECH network through its FEMTO-ST technological facility MIMENTO. The authors acknowledge Thomas Huot, Chencheng Tang, Mélissa Blot, Patrick Rougeot, Johnny Beaugrand and Miguel Suarez for their help in early developments and useful discussions.

---

[1] D. Xing, F. Liu, and D. Xu, "An efficient coordinated control strategy to handle randomized inclination in precision assembly," *IEEE Transactions on Industrial Informatics*, 2019.

[2] S. Liu, Y.-F. Li, and D. Xing, "Sensing and control for simultaneous precision peg-in-hole assembly of multiple objects," *IEEE Transactions on Automation Science and Engineering*, 2019.

[3] S. Scholz, A. Elkaseer, T. Müller, U. Gengenbach, and V. Hagenmeyer, "Smart modular reconfigurable fully-digital manufacturing system with a knowledge-based framework: example of a fabrication of microfluidic chips," in *IEEE International Conference on Automation Science and Engineering*, 2018, pp. 1012–1017.

[4] R. Matthey, G. Mileti, L. Stauffer, P. Giaccari, A. Pollini, and L. Balet, "Assembly technique for miniaturized optical devices: towards space qualification," in *International Conference on Space Optics*, vol. 10564, 2012.

[5] K. Aoki, H. T. Miyazaki, H. Hirayama, K. Inoshita, T. Baba, K. Sakoda, N. Shinya, and Y. Aoyagi, "Microassembly of semiconductor three-dimensional photonic crystals," *Nature materials*, vol. 2, no. 2, pp. 117–121, 2003.

[6] K. Rabenorosoa, C. Clévy, P. Lutz, A. N. Das, R. Murthy, and D. Popa, "Precise motion control of a piezoelectric microgripper for microspectrometer assembly," in *International Design Engineering Technical Conferences and Computers and Information in Engineering Conference*,

vol. 49033, 2009, pp. 769–776.

[7] A. Elkaseer, M. Salem, V. Hagenmeyer, and S. Scholz, "Vision system-based inspection and alignment of laminated polymer films for 3d-integration of microsystems," *IFAC-PapersOnLine*, vol. 52, no. 15, pp. 13–18, 2019.

[8] J. D. Wason, J. T. Wen, J. J. Gorman, and N. G. Dagalakis, "Automated multiprobe microassembly using vision feedback," *IEEE Transactions on Robotics*, vol. 28, no. 5, pp. 1090–1103, 2012.

[9] S. Bargiel, K. Rabenorosoa, C. Clévy, C. Gorecki, and P. Lutz, "Towards micro-assembly of hybrid moems components on a reconfigurable silicon free-space micro-optical bench," *Journal of Micromechanics and Microengineering*, vol. 20, no. 4, p. 045012, 2010.

[10] J. Agnus *et al.*, "Robotic microassembly and micromanipulation at femto-st," *Journal of Micro-Bio Robotics*, vol. 8, no. 2, pp. 91–106, 2013.

[11] Z. Chen, D. Zhou, H. Liao, and X. Zhang, "Precision alignment of optical fibers based on telecentric stereo microvision," *IEEE/ASME Transactions on Mechatronics*, vol. 21, no. 4, pp. 1924–1934, 2016.

[12] B. Komati, K. Rabenorosoa, C. Clévy, and P. Lutz, "Automated guiding task of a flexible micropart using a two-sensing-finger microgripper," *IEEE Transactions on Automation Science and Engineering*, vol. 10, no. 3, pp. 515–524, 2013.

[13] H. K. Chu, J. K. Mills, and W. L. Cleghorn, "Dual-arm micromanipulation and handling of objects through visual images," in *IEEE International Conference on Mechatronics and Automation*, 2012, pp. 813–818.

[14] E. Avci, C.-N. Nguyen, K. Ohara, M. Kojima, Y. Mae, and T. Arai, "Towards high-speed automated micromanipulation," in *IEEE International Conference on Robotics and Automation*, 2013, pp. 1718–1723.

[15] S. Liu and Y.-F. Li, "Precision 3-d motion tracking for binocular microscopic vision system," *IEEE Transactions on Industrial Electronics*, vol. 66, no. 12, pp. 9339–9349, 2019.

[16] S. Liu, Y.-F. Li, and X.-W. Wang, "A novel dual-probe-based micrograsping system allowing dexterous 3-d orientation adjustment," *IEEE Transactions on Automation Science and Engineering*, vol. 17, no. 4, pp. 2048–2062, 2020.

[17] F. Shen, F. Qin, Z. Zhang, D. Xu, J. Zhang, and W. Wu, "Automated pose measurement method based on multivision and sensor collaboration for slice microdevice," *IEEE Transactions*

on Industrial Electronics, vol. 68, no. 1, pp. 488–498, 2020.

[18] J.-Y. Zhang, Y. Liu, Y. Liu, and Y.-P. Hao, "Automatic microassembly method based on teaching playback and visual servo," in *IEEE International Conference on Information Science and Control Engineering*, 2017, pp. 878–882.

[19] L. Wang, J. K. Mills, and W. L. Cleghorn, "Automatic microassembly using visual servo control," *IEEE Transactions on Electronics packaging manufacturing*, vol. 31, no. 4, pp. 316–325, 2008.

[20] D. O. Popa, R. Murthy, and A. N. Das, "$m3$-deterministic, multiscale, multirobot platform for microsystems packaging: Design and quasi-static precision evaluation," *IEEE Transactions on Automation Science and Engineering*, vol. 6, no. 2, pp. 345–361, 2009.

[21] B. Komati, A. Kudryavtsev, C. Clévy, G. Laurent, B. Tamadazte, J. Agnus, and P. Lutz, "Automated robotic microassembly of flexible optical components," in *IEEE International Symposium on Assembly and Manufacturing*, 2016, pp. 93–98.

[22] C. Clévy, I. Lungu, K. Rabenorosoa, and P. Lutz, "Positioning accuracy characterization of assembled microscale components for micro-optical benches," *Assembly Automation*, 2014.

[23] W. Shang, H. Ren, M. Zhu, T. Xu, and X. Wu, "Dual rotating microsphere using robotic feedforward compensation control of cooperative flexible micropipettes," *IEEE Transactions on Automation Science and Engineering*, vol. 17, no. 4, pp. 2004–2013, 2020.

[24] H. Li, X. Zhang, S. Yao, B. Zhu, and S. Fatikow, "An improved template-matching-based pose tracking method for planar nanopositioning stages using enhanced correlation coefficient," *IEEE Sensors Journal*, vol. 20, no. 12, pp. 6378–6387, 2020.

[25] H. Bettahar, O. Lehmann, C. Clévy, N. Courjal, and P. Lutz, "6-dof full robotic calibration based on 1-d interferometric measurements for microscale and nanoscale applications," *IEEE Transactions on Automation Science and Engineering*, 2020.

[26] S. Yao, H. Li, S. Pang, B. Zhu, X. Zhang, and S. Fatikow, "A review of computer microvision-based precision motion measurement: Principles, characteristics, and applications," *IEEE Transactions on Instrumentation and Measurement*, vol. 70, pp. 1–28, 2021.

[27] P. Nazemzadeh, D. Fontanelli, D. Macii, and L. Palopoli, "Indoor localization of mobile robots through qr code detection and dead reckoning data fusion," *IEEE/ASME Transactions on Mechatronics*, vol. 22, no. 6, pp. 2588–2599, 2017.

[28] D. Kruse, J. T. Wen, and R. J. Radke, "A sensor-based dual-arm tele-robotic system," *IEEE*

Transactions on Automation Science and Engineering, vol. 12, no. 1, pp. 4–18, 2014.

[29] S. Basiratzadeh, E. D. Lemaire, M. Dorrikhteh, and N. Baddour, "Fiducial marker approach for biomechanical smartphone-based measurements," in *IEEE International Conference on Bioengineering for Smart Technologies*, 2019, pp. 1–4.

[30] E. Olson, "AprilTag: A robust and flexible visual fiducial system," in *IEEE International Conference on Robotics and Automation*, May 2011, pp. 3400–3407.

[31] S. Garrido-Jurado, R. Muñoz-Salinas, F. J. Madrid-Cuevas, and M. J. Marín-Jiménez, "Automatic generation and detection of highly reliable fiducial markers under occlusion," *Pattern Recognition*, vol. 47, no. 6, pp. 2280–2292, 2014.

[32] L. Belussi and N. Hirata, "Fast qr code detection in arbitrarily acquired images," in *IEEE Conference on Graphics, Patterns and Images*, 2011, pp. 281–288.

[33] Y. Gu and W. Zhang, "Qr code recognition based on image processing," in *IEEE International Conference on Information Science and Technology*, 2011, pp. 733–736.

[34] G. Klimek and Z. Vamossy, "Qr code detection using parallel lines," in *IEEE International Symposium on Computational Intelligence and Informatics*, 2013, pp. 477–481.

[35] F. J. Romero-Ramirez, R. Muñoz-Salinas, and R. Medina-Carnicer, "Speeded up detection of squared fiducial markers," *Image and vision Computing*, vol. 76, pp. 38–47, 2018.

[36] H. Shi, G. Sun, Y. Wang, and K.-S. Hwang, "Adaptive image-based visual servoing with temporary loss of the visual signal," *IEEE Transactions on Industrial Informatics*, vol. 15, no. 4, pp. 1956–1965, 2018.

[37] A. N. André, P. Sandoz, B. Mauzé, M. Jacquot, and G. J. Laurent, "Sensing one nanometer over ten centimeters: A micro-encoded target for visual in-plane position measurement," *IEEE/ASME Transactions on Mechatronics*, 2020.

[38] A. N. André, P. Sandoz, B. Mauzé, M. Jacquot, and G. J. Laurent, "Robust phase-based decoding for absolute (x, y, θ) positioning by vision," *IEEE Transactions on Instrumentation and Measurement*, 2020.

[39] T. J. Soon, "Qr code," *Synthesis Journal*, vol. 2008, pp. 59–78, 2008.

[40] D. Forsyth and J. Ponce, *Computer vision: A modern approach.* Prentice hall, 2011.

[41] C. McGray, C. R. Copeland, S. M. Stavis, and J. Geist, "Centroid precision and orientation precision of planar localization microscopy," *Journal of microscopy*, vol. 263, no. 3, pp. 238–249, 2016.

[42] N. Azizipour, R. Avazpour, D. H. Rosenzweig, M. Sawan, and A. Ajji, "Evolution of biochip technology: A review from lab-on-a-chip to organ-on-a-chip," *Micromachines*, vol. 11, no. 6, 2020.

[43] X. Huang, K. Torres-Castro, W. Varhue, A. Salahi, A. Rasin, C. Honrado, A. Brown, J. Guler, and N. S. Swami, "Self-aligned sequential lateral field non-uniformities over channel depth for high throughput dielectrophoretic cell deflection," *Lab on Chip*, vol. 21, pp. 835–843, 2021.

[44] V. Gauthier, A. Bolopion, and M. Gauthier, "Analytical formulation of the electric field induced by electrode arrays: Towards automated dielectrophoretic cell sorting," *Micromachines*, vol. 8, no. 8, p. 253, 2017.

[45] Y. Temiz, R. D. Lovchik, G. V. Kaigala, and E. Delamarche, "Lab-on-a-chip devices: How to close and plug the lab?" *Microelectronic Engineering*, vol. 132, pp. 156–175, 2015.

[46] E. Marchand, F. Chaumette, F. Spindler, and M. Perrier, "Controlling an uninstrumented manipulator by visual servoing," *The International Journal of Robotics Research*, vol. 21, no. 7, pp. 635–647, 2002.

[47] Z. Zhang, X. Wang, J. Liu, C. Dai, and Y. Sun, "Robotic micromanipulation: Fundamentals and applications," *Annual Review of Control, Robotics, and Autonomous Systems*, vol. 2, pp. 181–203, 2019.

[48] C. Clévy, M. Rakotondrabe, and N. Chaillet, *Signal measurement and estimation techniques for micro and nanotechnology.* Springer Science & Business Media, 2011.

[49] Q. Liang, D. Zhang, G. Coppola, Y. Wang, S. Wei, and Y. Ge, "Multi-dimensional mems/micro sensor for force and moment sensing: A review," *IEEE Sensors Journal*, vol. 14, no. 8, pp. 2643–2657, 2014.

[50] Y. Wei and Q. Xu, "An overview of micro-force sensing techniques," *Sensors and Actuators A: Physical*, vol. 234, pp. 359–374, 2015.

[51] B. P. Trease, Y.-M. Moon, and S. Kota, "Design of Large-Displacement Compliant Joints," *Journal of Mechanical Design*, vol. 127, no. 4, pp. 788–798, 11 2004.